agriculture

Article

Sensorless Design and Analysis of a Brushed DC Motor Speed Regulation System for Branches Sawing

Shangshang Cheng [1], Huijun Zeng [1], Zhen Li [1,2,*], Qingting Jin [1], Shilei Lv [1,2], Jingyuan Zeng [3] and Zhou Yang [4]

[1] College of Electronic Engineering (College of Artificial Intelligence), South China Agricultural University, Guangzhou 510642, China; chengshangshang@stu.scau.edu.cn (S.C.); zenghuijun@stu.scau.edu.cn (H.Z.); jinqingting@stu.scau.edu.cn (Q.J.); lvshilei@scau.edu.cn (S.L.)
[2] Division of Citrus Machinery, China Agriculture Research System, Guangzhou, 510642, China
[3] School of Computer Science, Jiaying University, Meizhou 514015, China; zengjingyuan@jyu.edu.cn
[4] Party and Government Office, Guangdong Ocean University, Zhanjiang 524088, China; yangzhou@scau.edu.cn
* Correspondence: lizhen@scau.edu.cn

Abstract: Saw rotational speed critically influences cutting force and surface quality yet is often destabilized by variable cutting resistance. The sensorless detection method for calculating rotational speed based on current ripple can prevent the contact of wood chips and dust with Hall sensors. This paper introduces a speed control system for brushed DC motors that capitalizes on the linear relationship between current ripple frequency and rotational speed. The system achieves speed regulation through indirect speed measurement and PID control. It utilizes an H-bridge circuit controlled by the EG2014S driver chip to regulate the motor direction and braking. Current ripple detection is accomplished through a 0.02 Ω sampling resistor and AMC1200SDUBR signal amplifier, followed by a wavelet transform and Savitzky–Golay filtering for refined signal extraction. Experimental results indicate that the system maintains stable speeds across the 2000–6000 RPM range, with a maximum error of 2.32% at 6000 RPM. The improved ripple detection algorithm effectively preserves critical signals while reducing noise. This enables the motor to quickly regain speed when resistance is encountered, ensuring a smooth cutting surface. Compared to traditional Hall sensor systems, this sensorless design enhances adaptability in agricultural applications.

Keywords: sensorless control; brushed DC motor; agricultural sawing; current ripple; branch sawing

check for updates

Citation: Cheng, S.; Zeng, H.; Li, Z.; Jin, Q.; Lv, S.; Zeng, J.; Yang, Z. Sensorless Design and Analysis of a Brushed DC Motor Speed Regulation System for Branches Sawing. *Agriculture* **2024**, *14*, 2078. https://doi.org/10.3390/agriculture14112078

Academic Editor: Dainius Steponavičius

Received: 20 October 2024
Revised: 14 November 2024
Accepted: 14 November 2024
Published: 19 November 2024

1. Introduction

Saw cutting is a critical process in agricultural production, used both for harvesting crops at maturity and for trimming during management periods. At the maturity stage, saw cutting is primarily used for the harvest of crops such as wheat, corn, and sugarcane, typically employing high-power, non-selective cutting methods [1,2]. Research in this area focuses on optimizing cutting parameters, including rotational speed, feed rate, and saw blade tooth geometry, to enhance operational efficiency and reduce energy consumption [3].

In selective cutting during crop management, such as cotton topping, tobacco topping, and pruning fruit tree branches [4–6], both efficiency and the smoothness of the cut surface are critical. Studies have shown that uneven cut surfaces increase the risk of fungal infections, which can negatively affect crop yield and quality [7,8]. The quality of saw cutting is closely tied to critical parameters, particularly rotational speed and feed rate. Variations in cutting resistance during the process can increase motor load or even cause stalling, making precise motor speed control essential for achieving high-quality cuts.

Brushed DC motors, as the primary power source for saw cutting speed, often experience significant reductions in speed when encountering resistance during operation. To ensure cutting efficiency and quality, precise monitoring and timely adjustment of motor speed are essential. Traditional control methods for brushed DC motors are typically divided into sensor-based and sensorless control techniques. Sensor-based control typically requires the installation of an optical encoder or Hall-effect sensor at the rear of the motor to measure rotational speed via pulse signals generated by the sensor [9]. However, the high-intensity nature of saw cutting operations in agricultural environments often necessitates frequent motor maintenance or replacement, and the installation of Hall sensors significantly increases operational costs. Moreover, sensor performance is highly susceptible to environmental factors such as humidity and dust. Sensorless control methods are generally classified into circuit model-based and current ripple-based detection techniques. Circuit model-based control treats the brushed DC motor as an equivalent series circuit of resistance and inductance, estimating motor speed by inputting parameters such as voltage, current, resistance, and inductance [10]. However, these parameters are not constant in practical applications and reduce the reliability of the model.

Current ripple arises during motor operation due to the periodic connection and disconnection of current in the windings, a consequence of the commutator rotating and making contact with the brushes. By exploiting the periodic variations in current ripple, speed estimation can be performed without the need for specific motor parameters, providing critical information on rotor speed. Ramli [11] applied an adaptive filter for speed estimation, while Vazquez-Sanchez [12] employed a support vector machine (SVM) to estimate motor speed by detecting the inverse distance between pulses, combined with pulse counting for position estimation. Radcliffe and Kumar [13] introduced a speed estimation method based on measuring inductive spikes when the motor is de-energized. Vazquez-Sanchez [14] achieved an error margin of less than 1 RPM within the 2000–3000 RPM range by analyzing current spectral components and detecting speed changes within 2 s. Nemec [15] further demonstrated the application of current peak processing with analog and digital filtering to achieve electronic odometry for mobile robots.

Additionally, application notes published by Texas Instruments [16] and Microchip [17] introduced ripple-counting techniques for speed estimation. These methods estimate rotor position using pulse signals and employ open-loop control to adjust motor voltage. Zhang [18] presented an enhanced Kalman filter that integrates results from both ripple-based and model-based estimations. Vidlak [19] developed a discrete filter with a floating bandwidth to process extracted ripple components, estimating their frequency to infer motor speed, which is subsequently used as feedback for the speed controller.

The aforementioned method estimates motor speed by processing current ripple signals and employing noise reduction techniques, constructing a closed-loop control system capable of meeting motor speed calculation requirements in constant-speed scenarios. However, in branch sawing applications, the mechanical properties of branches are closely related to their fiber distribution, and the diverse natural growth patterns of branches result in complex and variable sawing resistance. Branch sawing operates under a single-support condition, with typical sawing speeds between 3000 and 6000 rpm. High-speed sawing induces vibrations that can lead to blade pinching, causing instability in sawing force [20,21]. Furthermore, as the cutting volume per unit time increases, sawing resistance also rises, impacting sawing speed [22]. Compared to Hall sensors, sensorless control avoids the need for data transmission between sensors, enabling real-time detection of speed fluctuations caused by resistance changes during sawing. This reduces motor speed detection time to the millisecond level, thereby achieving more effective constant-speed control.

This paper proposes a current ripple-based control method for brushed DC motors, using estimated speed as feedback for sensorless regulation. The cascaded structure integrates speed and current controllers, enabling precise control in agricultural saw cutting applications. This approach effectively addresses stalling issues, enhances operational efficiency, and reduces the risk of disease from uneven cuts, ultimately improving agricultural productivity.

2. Materials and Methods

2.1. Ripple Current Extraction and Noise Analysis

2.1.1. Brushed DC Motor Structure

The basic structural model of a brushed DC motor is shown in Figure 1, with key components and their operational principles clearly depicted. The red and blue sections indicate the north (N) and south (S) poles of the permanent magnet, respectively. Positioned between these poles, the coil abcd forms the rotor's armature winding, while the yellow semicircles represent the motor's commutator. When the DC power supply is connected, current flows through brush A into the coil abcd. According to Lorentz law, the coil experiences a Lorentz force in the magnetic field, producing torque that drives the rotor to rotate counterclockwise. As the rotor turns, brushes A and B contact different sections of the commutator, automatically reversing the direction of current flow through the armature winding. This design of the commutator ensures that the coil abcd is continuously subjected to torque within the magnetic field, allowing the rotor to rotate steadily. This mechanism enhances both the operational efficiency and stability of the motor.

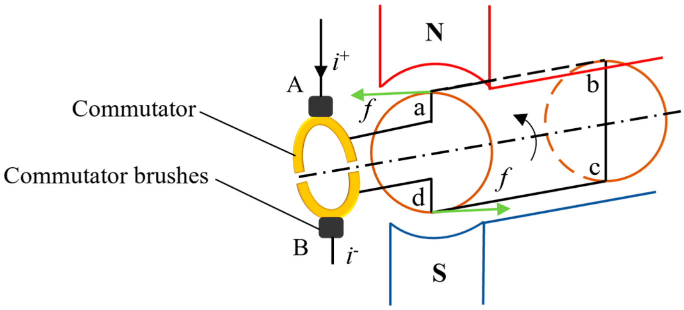

Figure 1. Structural model of brushed DC motor.

2.1.2. Current Ripple

In practical motor structures, the armature winding usually consists of multiple coils, which vary based on the application scenario. The rotor connects to the external circuit via brushes and a commutator. According to Faraday's law of electromagnetic induction, as the motor rotates, each coil generates a back electromotive force (back-EMF). This back-EMF aids in switching the current direction through the brushes and commutator, indirectly achieving rectification and transmitting current to the external circuit.

During the operation of a brushed DC motor, brushes contact different commutator segments, causing variations in armature current. This creates a ripple current, which appears as a pulsation superimposed on the DC component and resembles a sinusoidal waveform [23].

2.1.3. Current Ripple Characteristics

The characteristics of current ripples are closely linked to the motor's structural parameters, with ripple amplitude influenced by factors such as the number of coils, coil inductance, and motor power. Additionally, the frequency of the ripple components depends on the rate of current fluctuations. Yuan [24] established a relationship between ripple frequency and the motor's rotational speed, as represented by the Equation (1).

$$f_r = \frac{cpkn_m}{60} \tag{1}$$

where fr represents the ripple frequency, p is the number of pole pairs in the motor, n_m is the rotational speed of motor, k is the number of commutator segments, and c is the parity coefficient. When the number of commutator segments k is even, c = 1; when k is odd, c = 2. According to Equation (1), p, k, and c are all structural parameters of the motor. Once the motor model is selected, these parameters remain constant and are not affected by external factors such as temperature, humidity, or operational duration. Experimental verification of the 775 brushed DC motor reveals that its number of pole pairs is 5. Substituting this into Equation (1), the relationship between rotational speed and frequency for this motor is derived, as shown in Equation (2).

$$n_m = 6 \cdot f_r \tag{2}$$

The ripple frequency is directly proportional to the motor's rotational speed, providing a basis for using ripple signals to estimate speed. These signals can replace Hall pulse signals for speed estimation, offering a simpler alternative that avoids the complexities of inductance-based mathematical models, which can be affected by variations in armature coil resistance, number of turns, and magnetic properties.

2.1.4. Ripple Noise Extraction

In the method of calculating motor speed based on ripple frequency, once the motor model is determined, the armature ripple current becomes the sole independent variable. Therefore, understanding the causes and patterns of noise formation is a prerequisite for accurately processing ripple signals. In the experiment, the loop current signal was transmitted to a ZLG ZDS2024plus oscilloscope (sampling frequency of 200 MHz, Zhiyuan Electronics, Guangzhou, China) using the CP2100X high-frequency AC/DC current probe (sampling frequency of 300 kHz, accuracy of 1 mA, MICSIG Shenzhen, China). The current ripple signal extracted at a sampling frequency of 10 kHz, when the rotational speed was 3000 rpm, is shown in Figure 2. As depicted, the overall current ripple of the motor exhibits periodic variations over time; however, the details reveal significant noise. Close examination in the magnified sections shows that spikes cause false peak values in the signal. Additionally, the extracted ripple signal displays a certain bandwidth rather than a smooth curve, which is attributable to the use of pulse width modulation (PWM) power supply.

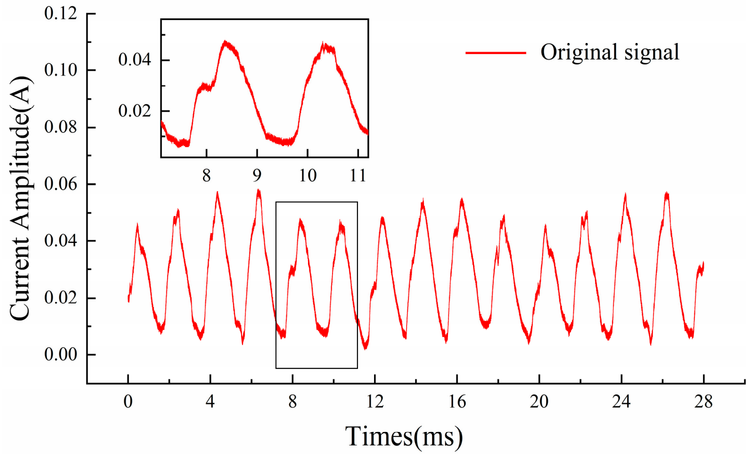

Figure 2. Original ripple signal of brushed DC motor.

Figure 2 shows that spikes in the ripple periodic signal are concentrated around the peak regions, primarily influenced by the motor's structure and operational environment. Poor contact between the brushes and the commutator is a significant factor; unstable contact can interrupt current flow or cause fluctuations in contact resistance, leading to spikes. Additionally, mechanical vibrations or brush wear during high-speed operation can cause bouncing at the contact points, further increasing spike occurrence. As the surfaces of the brushes and commutator wear, uneven contact can lead to irregular current distribution, heightening the likelihood of spikes. Additionally, electromagnetic interference (EMI), high-frequency noise, and transient disturbances in the power supply can distort the ripple signal [25]. Mechanical vibrations, internal motor imbalances, and external vibration sources can further affect brush-commutator contact, exacerbating the spike phenomenon within the ripple signal.

2.2. System Design and Circuit Implementation

2.2.1. Reduction in Current Ripple Noise

Analyzing the operating principles of brushed motors reveals that noise in the form of spikes within the ripple signal is inevitable. Consequently, accurately analyzing the ripple signal requires the application of filtering techniques to the ripple current. Given that the ripple current signal in the armature is time-domain data, time-frequency analysis methods are essential for eliminating internal noise and extracting the ripple period. While Fourier transform (FT) and fast Fourier transform (FFT) effectively capture the frequency-domain characteristics of the current signal, they offer only a global frequency-domain description [26]. To quickly and accurately identify variations in motor speed, it is crucial to focus on the local time-frequency features of the signal, necessitating the acquisition of energy distribution in the time-frequency space through time-frequency transformation. The short-time Fourier transform (STFT) decomposes the current signal into equal-length time segments using a fixed window function, extracting the frequency-domain characteristics of each segment. However, this fixed window approach limits resolution flexibility. In contrast, wavelet transform employs a variable basis function, allowing for the rapid identification of sudden signal changes, as expressed in Equation (3).

$$CWT\varphi(a,b) =< \varphi(t), \Phi_{a,b}(t) >= a\frac{1}{2}\int_{-\infty}^{+\infty} \varphi(t)\overline{\Phi\left(\frac{tb}{a}\right)}dt \tag{3}$$

By discretizing the scale factor $a = a_0^{\tau}, (\tau \in Z)$, while keeping the time-shift factor continuous, a semi-discrete dyadic wavelet transform is derived. This discrete form of the wavelet transform achieves scale discretization through signal decomposition and reconstruction, which enhances computational efficiency. Meanwhile, it preserves time-domain continuity, ensuring time-shift invariance. This approach enables efficient time-frequency analysis and signal compression. The standard expression for this transform is provided in Equation (4).

$$DWT_{\phi}(\tau,b) =< \varphi(t), \Phi_{\tau,b}(t) >= \int \varphi(t)\overline{\Phi_{\tau,b}(t)}dt \tag{4}$$

The Savitzky–Golay (S-G) filter smooths signals by fitting a polynomial using the least-squares method, preserving key features such as extrema and width. It is particularly effective for reducing low-frequency noise in ripple signals, which is crucial for enabling accurate extremum detection in wavelet transforms. The S-G filter performs polynomial fitting over a sliding window of data, with the central value retained as the filtered result. The core of the method lies in the real-time computation of the data weight coefficient matrix. Assuming that at least 2n data points are required for wavelet multi-resolution decomposition of the ripple current signal, the filtering result at sampled time k is expressed by Equation (5).

$$\varphi'(i) = \begin{cases} \varphi(i), & k < 2^n \\ x(i), & k = 2^n \\ \varphi'(k+1) = x(k+1), & k = 2^n + 1 \end{cases} \tag{5}$$

Let the data window width be defined as n = 2K + 1, where K is an integer, and the data to be processed is denoted as A, with a total length of L. The data within the window is represented as x. By fitting a polynomial of degree j to the matrix x, the fitted values for each point within x can be obtained as follows

$$\hat{X}_k = c_0 + c_1k + \cdots + c_jk^j, -K \leq k \leq K \tag{6}$$

$$S = \left[s_0, s_1, \cdots, s_j\right] = \left[k^0, k^1, \cdots, k^j\right] \tag{7}$$

The matrix of $\hat{X}$ is derived in Equation (8).

$$\hat{X} = \sum_{i=0}^{j} S_i C_i = \begin{bmatrix} s_0 & s_1 & \cdots & s_j \end{bmatrix} \begin{bmatrix} c_0 \\ c_1 \\ \vdots \\ c_j \end{bmatrix} = SC \tag{8}$$

The polynomial coefficient matrix C corresponds to the value when the squared error of the least-squares fitting reaches its minimum.

$$v = \sum_{k=-K}^{K} e_k^2 = \sum_{k=-K}^{K} \left[X_k - \hat{X}_k\right]^2 = \sum_{k=-K}^{K} \left[X_k - \left(c_0 + c_1 k + \cdots + c_j k^j\right)\right]^2 = \min v \tag{9}$$

By simplifying Equation (9), $e_k^2 = \left(X_k - \hat{X}_k\right) = \left(X_k - SC\right)^2 = \min$ is obtained, Expressing e_k^2 in matrix form results in Equation (10).

$$e_k^2 = e_k^T e_k = X_k^T X_k - 2C^T S^T X_k + C^T S^T S C = \min \tag{10}$$

Simplifying Equation (10) yields $\frac{\partial e_k^2}{\partial C} = -2S^T e_k = 0$, leading to the expression for the coefficient matrix C in Equation (11).

$$C = \left(S^T S\right)^{-1} S^T X_k = G^T X_k \tag{11}$$

By substituting the coefficient matrix C into Equation (8), it can be obtained that:

$$\hat{x}_k = SC = S\left(S^T S\right)^{-1} S^T X_k = D x_k \tag{12}$$

The time-frequency analysis of motor ripple current using wavelet transform follows four key stages: sampling, decomposition, coefficient processing, and reconstruction, as depicted in Figure 3. For the 775 brushed DC motor operating within an agricultural context, with a rotational speed range of 2000–6000 rpm, the maximum frequency reaches 1000 Hz. In this study, a sampling frequency of 10 kHz was applied. After sampling, a suitable wavelet basis function is selected to perform the inner product on the signal, followed by iterative decomposition using the wavelet formula. This process generates multi-level wavelet coefficient matrices for the current signal. Biorthogonal quadratic spline wavelets, valued for their orthogonality and symmetry, are particularly effective for extracting the periodic components of the ripple signal and detecting extrema.

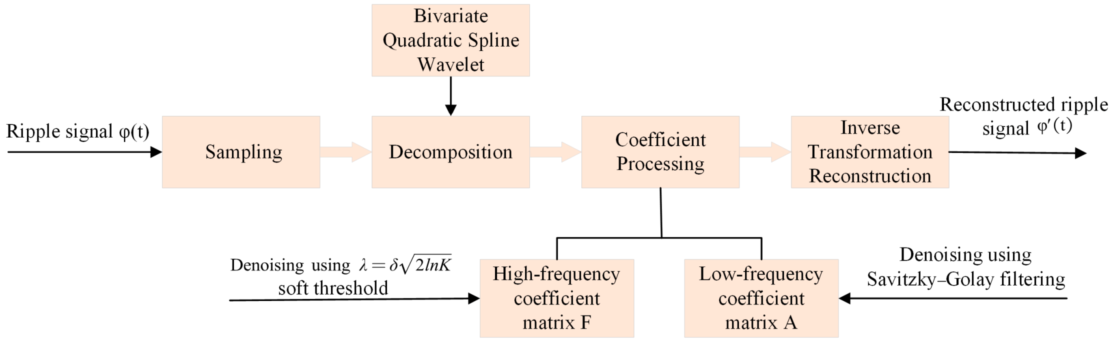

Figure 3. Noise reduction process for motor current ripple.

As shown in the construction of the biorthogonal quadratic spline wavelet Formula (13), the low-pass filter coefficient matrix is $E_0 = \begin{bmatrix} 1/4 & 3/4 & 3/4 & 1/4 \end{bmatrix}^T$, and the high-pass filter coefficient matrix is $E_1 = \begin{bmatrix} -1/4 & -3/4 & 3/4 & 1/4 \end{bmatrix}^T$. First, perform a binary wavelet transform on the original signal φ(t), decomposing it into four levels to obtain the high-frequency coefficient matrix F and the approximation coefficient matrix A [i]. For the high-frequency coefficient matrix F, apply soft thresholding with a threshold value $\lambda = \delta\sqrt{2InK}$ for denoising. For the approximation coefficient matrix A, the Savitzky–Golay (S-G) filtering algorithm is applied. The core of S-G filtering lies in solving the matrix D, which requires only the window size n and the polynomial degree j as input parameters. The polynomial coefficient matrix D can be calculated, and combined with Equation (6), the filtered signal data can be obtained. By choosing a polynomial degree of j = 3 and a window size of n = 128, high-frequency noise can be effectively reduced.

$$\begin{array}{l} H_0(z) = \frac{1+3z^{-1}+3z^{-2}+z^{-3}}{4} \\ H_1(z) = \frac{-1-3z^{-1}+3z^{-2}+z^{-3}}{4} \end{array} \tag{13}$$

2.2.2. Wavelet Transform Detection of Ripple Signal Extreme Points

The binary wavelet transform is utilized to detect the peak values of ripple signals, employing a method that parallels singularity detection of the signal. However, the distinction lies in that singularity detection aims to pinpoint abrupt changes in the signal, while peak value detection focuses on identifying stable positions of the signal. Based on the wavelet transform Formula (4), it can be deduced that the result of the wavelet transform corresponds to the output value of the signal after being processed through a specific system, with the system impulse response denoted as $\Phi_{a,b}(t)$.

Let $\rho(t)$ be the smoothing function, which can be regarded as a low-pass filter, commonly represented by a Gaussian function. Define $\rho_a(t) = a^{\frac{1}{2}}\rho\left(\frac{t}{a}\right)$; thus, the wavelet can be expressed using the function $\rho(t)$ as follows:

$$\Phi^{(1)}(t) = \frac{d\rho(t)}{dt} \tag{14}$$

$$\Phi^{(2)}(t) = \frac{d^2\rho(t)}{dt} \tag{15}$$

The original signal $\varphi(t)$ undergoes wavelet transformation through the mother wavelets $\Phi^{(1)}(t)$ and $\Phi^{(2)}(t)$, resulting in Equations (16) and (17).

$$CWT_{\varphi}^{(1)}(t) = \varphi(t) * \Phi^{(1)}(t) = a\frac{d}{dt}[\varphi(t) * \rho_a(t)] \tag{16}$$

$$CWT_{\varphi}^{(2)}(t) = \varphi(t) * \Phi^{(2)}(t) = a^2\frac{d^2}{dt}[\varphi(t) * \rho_a(t)] \tag{17}$$

Through Formulas (16) and (17), it is known that the CWT coefficients $CWT_{\varphi}^{(1)}(t)$ and $CWT_{\varphi}^{(2)}(t)$ obtained from the original signal after wavelet transformation are proportional to the first-order derivative and second-order derivative of $\varphi(t) * p_a(t)$ respectively, and the zero points of $CWT_{\varphi}^{(1)}(t)$ correspond to the extrema of the original signal, while the zero points of $CWT_{\varphi}^{(2)}(t)$ correspond to the inflection points of the original function. When the wavelet function is considered the first-order differential of a smooth function, the zero points of the wavelet transform of the signal correspond to the extrema of the original signal; when the wavelet function is considered the second-order differential of a smooth function, the zero points of the coefficient obtained after the transformation are the singular points of the original signal. That is, by using a specific wavelet for the second-order wavelet transform, the extrema of the signal correspond to the points where $CWT_{\varphi}^{(1)}(t) = 0$.

2.2.3. PWM Voltage Regulating and Speed Stabilizing System Design

After applying the improved wavelet transform, the ripple signal was precisely extracted, enabling accurate detection of the rotational speed and its variation trends during the sawing process. This serves as a foundation for real-time speed control adjustments. As depicted in Figure 4, motor speed is controlled by adjusting the pulse width modulation (PWM) duty cycle, ensuring it aligns with the target speed.

During the startup phase, the PWM duty cycle gradually increases, allowing the motor to smoothly accelerate to the desired speed. Throughout sawing, any increase in cutting resistance causes a speed reduction. The wavelet-based speed estimator continuously monitors these speed fluctuations in real time, feeding the deviation from the target speed into a proportional–integral (PI) controller. The controller then adjusts the PWM duty cycle, increasing the motor voltage to restore the desired speed. This closed-loop control strategy significantly enhances system responsiveness, ensuring both stability and accuracy of the motor's rotational speed during operation. It also allows timely adjustments to accommodate load changes, thereby maintaining the continuity and efficiency of the sawing process.

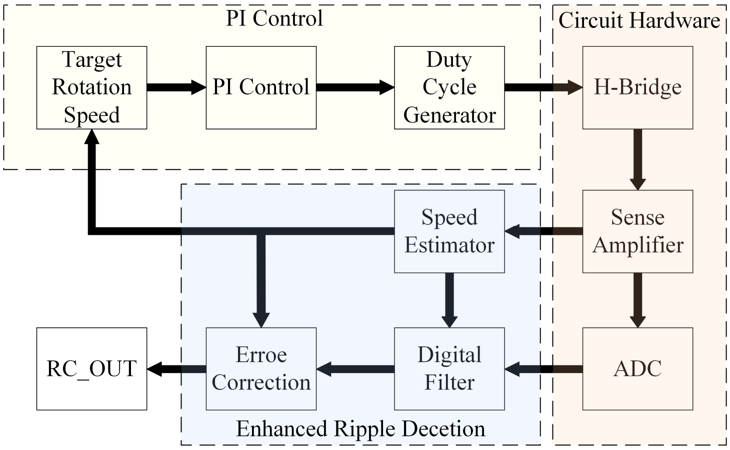

Figure 4. Brushed DC motor speed stabilisation system design.

2.2.4. Critical Circuit Design

An H-bridge circuit was designed using two EG2014S half-bridge driver chips to control four MOSFETs, as shown in Figure 5. The EG2014S chip processes input logic signals, performs output level conversion, and manages dead time control. When the main control chip sends control signals, the EG2014S adjusts the switching states of the MOSFETs based on these signals, enabling current switching across the motor terminals and thus altering the motor's operating state. The PWM1/2_IN signals control motor speed and are connected to pins PA8 and PA9 of the main chip, while SD_IN serves as the logic control signal from the main chip, connected to pin PG12. The control signals from the main chip are opto-isolated before being transmitted to the input pins of the EG2014S to protect the main chip from potential damage due to high voltage or current.

To accurately calculate motor speed from the ripple frequency of the motor current, precise sampling of the current signal is crucial. Since the ripple signal amplitude is much smaller than the direct current component and susceptible to external interference, an operational amplifier circuit is used for signal amplification and noise reduction. As shown in Figure 6, a 0.02 Ω, 2 W sampling resistor is placed in series with the current output terminal of the H-bridge driver circuit to convert the current into a voltage signal. The AMC1200SDUBR (Texas Instruments, Dallas, TX, USA) isolation op-amp then amplifies this voltage signal by a factor of eight, outputting it in differential form.

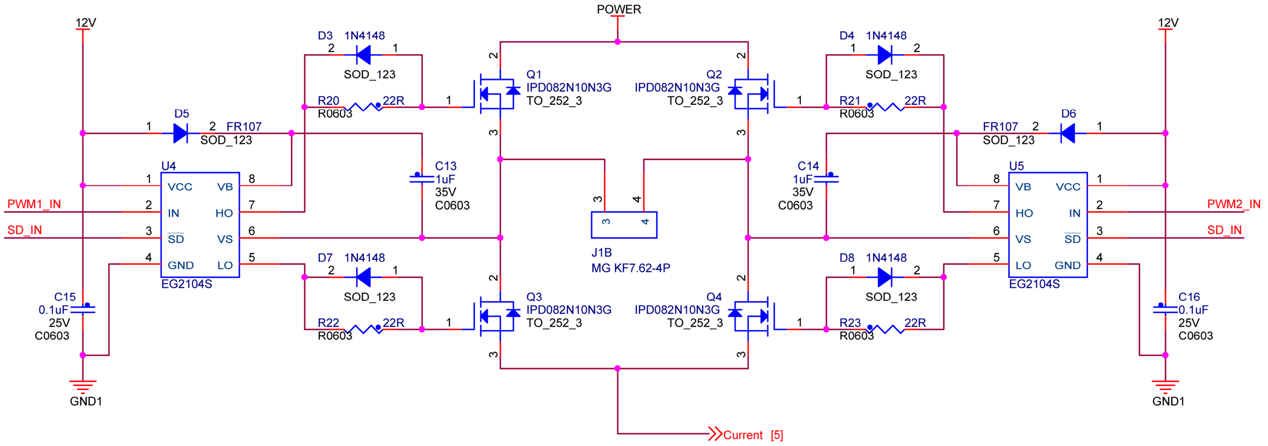

Figure 5. H-bridge drive circuit for brushed DC motor.

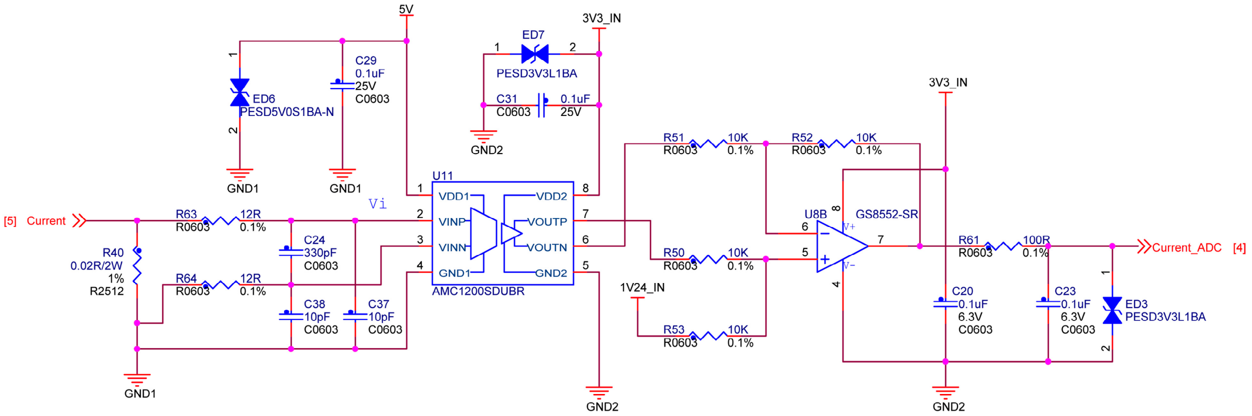

Figure 6. Ripple current detection circuit.

The amplified ripple current signal is preprocessed through a filtering circuit before being digitized by the ADC module of the STM32F407C8T6 (STMicroelectronics, Geneva, Switzerland) microcontroller. Using wavelet transformation combined with a Savitzky–Golay (S-G) filter, stable ripple components are extracted. An extremum detection algorithm based on wavelet transformation is applied to calculate the ripple period. This data, along with direct current measurements, are fed into the controller for further analysis, enabling precise motor speed calculation.

3. Results

3.1. Signal Noise Reduction Analysis

To validate the effectiveness of the improved wavelet threshold denoising algorithm, it was applied to the extracted ripple data, with the results shown in Figure 7. The algorithm successfully removed spikes and false peaks, significantly improving the overall signal quality. Compared to the original signal, the improved method effectively eliminated noise while preserving critical features such as peak positions, amplitude variations, and the overall waveform trend. This demonstrates that the algorithm strikes a good balance between noise reduction and signal fidelity, maintaining the integrity of the signal. These results confirm the algorithm's reliability and effectiveness in practical applications.

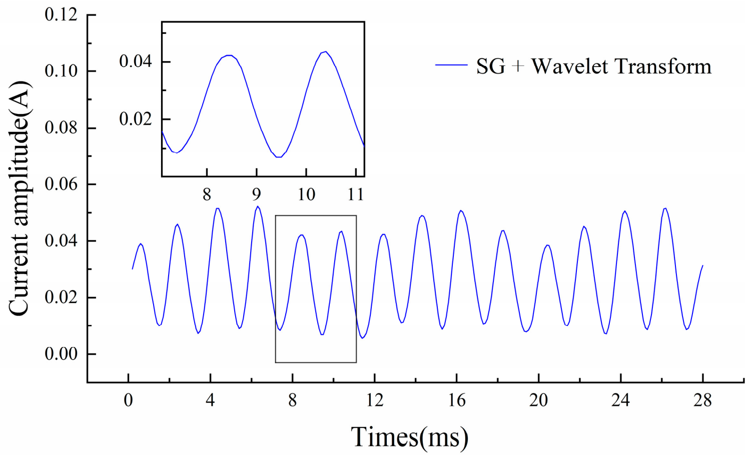

Figure 7. Improved wavelet denoising of ripple signals.

3.2. Motor Speed Stabilization Test Method

In agricultural sawing applications, cutting speed and feed rate are critical factors influencing cutting force and overall cutting quality, assuming constant saw blade structural parameters. When the feed rate remains constant and cutting speed decreases, the volume of material removed per unit time increases, resulting in higher cutting forces.

To evaluate the operational range of the proposed steady-speed control method, a sawing experimental platform was developed. As shown in Figure 8, the platform consists of a Cartesian coordinate frame constructed from aluminum profiles, a lead screw module, a 57-type stepper motor with its driver, a fixture, a circular saw blade (Dong Cheng, 4 × 30T), and a 775 brushed DC motor. Due to the variability in branch fiber distribution and the irreproducibility of experimental materials, a Hall sensor was used to collect speed data for assessing the performance of the control system. A Hall sensor with a resolution of 16, operating at 100 kHz, was installed at the motor's tail to analyze speed data and validate the effectiveness of the proposed steady-speed control method.

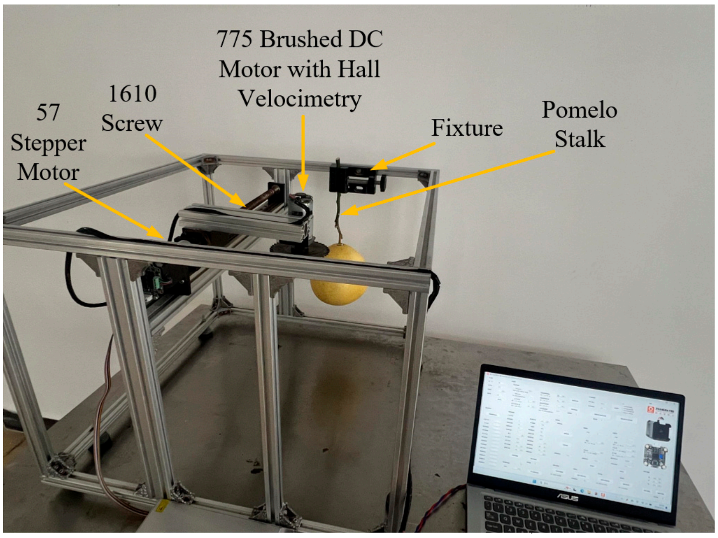

Figure 8. Sawing experimental platform.

3.3. Motor Speed Stabilization Analysis

In the motor sawing resistance experiments conducted on the experimental platform, we collected signals for voltage, current, and the Hall sensor located at the rear of the motor to analyze the temporal trends of these parameters. As illustrated in Figure 9, the red solid line represents voltage, the blue dashed line indicates current, and the green dotted line corresponds to cutting speed. The experimental results reveal that, upon closing the circuit, the current rapidly reaches an initial peak value before declining and stabilizing, while the motor speed increases swiftly. Once the speed reaches approximately 3000 RPM, the current stabilizes as well. During the initial stage of sawing, the cutting resistance causes a sharp decrease in motor speed, leading to a reduction in back electromotive force (back EMF) and a simultaneous decrease in voltage across the motor terminals. At the same time, as the motor encounters resistance, the current increases, and the voltage drop (IR drop) caused by the current flowing through the internal resistance of the motor further lowers the voltage across its terminals. Additionally, the increase in current results in greater energy loss in the form of Joule heating. To overcome the cutting resistance, the PWM control compensates for the decrease in speed by increasing the voltage across the motor terminals. However, due to the reduction in back EMF, the increase in voltage is not significant.

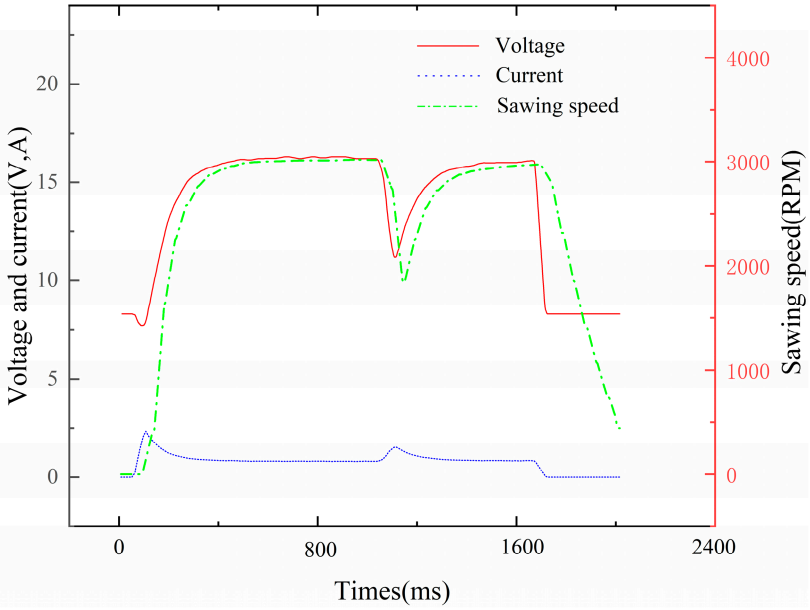

Figure 9. Variation of voltage, current, and speed during resistance and stabilization.

Notably, the voltage trough occurs before the speed trough, indicating that even when the voltage rises, the motor speed continues to decline, reflecting that the effect of back EMF counteracts part of the PWM boosting effect. As the PWM control voltage is further increased, the motor speed gradually recovers after reaching the trough. Subsequently, the closed-loop control system adjusts the PWM pulse width to ensure a smooth voltage transition, avoiding significant voltage fluctuations and thus ensuring stable motor operation. This control strategy effectively maintains motor performance under load conditions, ensuring the continuity and efficiency of the sawing process.

To further investigate the applicability of the proposed speed control method for the sawing motor, experiments were conducted at rotational speeds of 2000, 3000, 4000, 5000, and 6000 RPM. The speeds obtained from processing the ripple sampling data were compared with measurements from the Hall sensor located at the rear of the motor. The experimental results are illustrated in Figure 10, which lists the experimental conditions in descending order: 6000, 5000, 4000, 3000, and 2000 RPM.

From the analysis of the speed control effectiveness at different rotational speeds, it was observed that as the speed increased, the error of the proposed speed measurement method also increased. This rise in error is primarily attributed to poor contact of the carbon brushes and motor vibrations at higher speeds. When the motor encounters resistance, the magnitude of speed reduction is relatively small, resulting in a lower relative value at the trough. Furthermore, at higher speeds, the slope of the speed decrease after encountering resistance is relatively gentle. This phenomenon can be explained by the fact that, for the same motor, higher speeds correspond to greater power output. Consequently, when faced with the same cutting resistance, high-speed motors exhibit a greater power reserve.

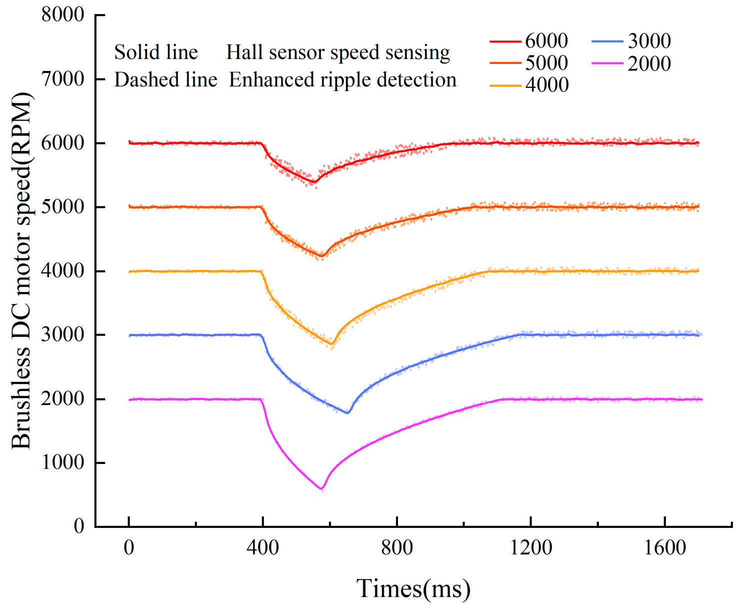

Figure 10. Performance comparison of steady-speed system.

In terms of the steady-state performance at specific rotational speeds, prior to encountering resistance during cutting, the improved scatter distribution from the ripple detection method in this study closely aligns with the speed measurement results obtained from the Hall sensor. When resistance is encountered, the error in the predicted speed slightly increases; however, after the completion of cutting, although the speed error decreases, it remains above the level observed before cutting commenced. This phenomenon can be attributed to the complex vibrations during the cutting process, as well as the minor residual vibrations of the motor driving the saw blade after cutting has concluded.

Data analysis revealed that the maximum error occurred during the cutting process at 6000 RPM, with an error margin of 2.32%, which meets the requirements for steady-speed control. Compared with conventional Hall sensors, the improved ripple velocity measurement method proposed in this study not only offers similar performance, but also eliminates the need to install additional sensors, which greatly simplifies system deployment and maintenance, and is particularly suitable for complex and changing agricultural environments. However, it is worth noting that although the method shows good application prospects, its performance under extreme conditions or when facing special materials still needs to be further verified. In addition, how to further reduce the control error under high-speed operation through optimization algorithms will be an important direction for future research. In conclusion, this innovative speed control strategy provides new possibilities for improving the efficiency of agricultural sawing operations, and also provides a certain reference value for the speed control of other types of motors in related fields.

4. Discussion

As shown in Figure 10, the system achieved stable speed control at various rotational speeds through a PID control strategy, though the speed regulation error increased as motor speed rose. This trend is consistent with the findings of Vazquez-Sanchez [14], who reported achieving control accuracy with an error below 1 RPM in the 2000–3000 RPM range. However, the error observed in this study was slightly higher in the same range, which can be attributed to the consideration of vibration effects caused by resistance changes during the sawing process. Unlike previous studies that typically focused on motor speed measurements under no-load or stable-load conditions, this study specifically addressed real operating conditions in agricultural sawing tasks. At high speeds, the instability of brush contact and the increased motor vibrations make speed estimation more challenging, leading to an increase in errors. This trend is consistent with the findings of Hosfeld [27]. The maximum error at 6000 RPM was 2.32%, which remains within an acceptable range. This result validates the effectiveness of current ripple-based detection, which provides reasonably accurate speed feedback even during the frequent and substantial changes experienced during sawing. Moreover, compared to traditional Hall sensor systems, the sensorless approach proposed in this study eliminates the need for additional sensor installations, simplifying the system and enhancing its adaptability and reliability in complex agricultural environments.

The brushed DC motor speed control system demonstrated strong performance, maintaining cutting efficiency while effectively addressing speed fluctuations caused by external disturbances. Future research could focus on optimizing signal processing algorithms to reduce noise interference and improve speed estimation accuracy, particularly at higher operating speeds. Hosfeld and Konigorski proposed a method to dynamically adjust the filter frequency based on motor speed, using an iterative approach to enhance the accuracy of speed calculations at high speeds [10]. Additionally, exploring more advanced control strategies, such as adaptive PID or fuzzy logic control, could further improve the system's responsiveness and stability under dynamic conditions. Khoo proposed an algorithm that integrates adaptive pulse detection, adaptive BEMF detection, and adaptive Kalman filtering to enhance the accuracy of sensorless speed detection under various operating conditions, such as acceleration, deceleration, coasting, and braking [28]. Nosheen introduced a control strategy based on non-integer differential-integral equations for sensorless speed control of induction motors, achieving a system delay significantly smaller than that of PID-controlled systems [29]. However, while optimizing algorithms and strategies, it is crucial to also ensure the real-time performance of the system.

5. Conclusions

Through an in-depth investigation of the application of brushed DC motors in agricultural sawing scenarios, this study presents a sensorless motor speed control method based on current ripple detection. This approach indirectly measures motor speed by extracting the ripple components from the motor current and employs a PID adjustment strategy to achieve effective control of the motor speed. Experimental results indicate that this method enables stable motor speed control across a range of 2000 to 6000 RPM, particularly when the motor encounters cutting resistance that causes a decrease in speed. In such instances, PWM modulation increases the voltage across the motor, restoring the target speed. As the rotational speed increases, the control error tends to rise, primarily due to unstable brush contact and motor vibrations at higher speeds. Moreover, the improved ripple speed measurement method demonstrates performance comparable to that of traditional Hall sensor measurements but offers greater practical value in complex agricultural environments due to the absence of the need for additional sensor installation, thereby simplifying system maintenance and usage.

Author Contributions: Conceptualization, S.C. and Z.L.; methodology, S.C. and S.L.; software, S.C. and H.Z.; validation, Z.Y., J.Z., and Q.J.; formal analysis, H.Z. and Q.J.; investigation, S.C.; resources, S.C.; data curation, Q.J.; writing—original draft preparation, S.C.; writing—review and editing, S.C.; visualization, H.Z.; supervision, Z.L.; project administration, Z.L., Z.Y. and S.L. All authors have read and agreed to the published version of the manuscript.

Funding: This research was funded by the open competition program of the top ten critical priorities of Agricultural Science and Technology Innovation for the 14th Five-Year Plan of Guangdong Province (2024KJ27). The authors sincerely acknowledge the members of the research team for their help.

Institutional Review Board Statement: Not applicable.

Data Availability Statement: The datasets used and/or analyzed during the current study are available from the corresponding author on reasonable request.

Conflicts of Interest: The authors declare no conflicts of interest.

References

1. Paixao, C.S.S.; Voltarelli, M.A.; de Oliveira, L.P.; Bernache, L.; Silva, R.P. Wear Quantification of Basal Cutting Knives in Sugarcane Harvesting. *Eng. Agric.* **2019**, *39*, 498–503. [CrossRef]
2. Paulo Testa, J.V.; Battistuzzi Martins, M.; Carpes Marques Filho, A.; Pereira Lancas, K.; Lustosa Sobrinho, R.; Finatto, T.; Okla, M.K.; AbdElgawad, H. Continuous and Impact Cutting in Mechanized Sugarcane Harvest: Quality, Losses and Impurities. *Agriculture* **2023**, *13*, 1329. [CrossRef]
3. Lenaerts, B.; Aertsen, T.; Tijskens, E.; De Ketelaere, B.; Ramon, H.; De Baerdemaeker, J.; Saeys, W. Simulation of Grain-Straw Separation by Discrete Element Modeling with Bendable Straw Particles. *Comput. Electron. Agric.* **2014**, *101*, 24–33. [CrossRef]
4. Botterill, T.; Paulin, S.; Green, R.; Williams, S.; Lin, J.; Saxton, V.; Mills, S.; Chen, X.; Corbett-Davies, S. A Robot System for Pruning Grape Vines. *J. Field Robot.* **2017**, *34*, 1100–1122. [CrossRef]
5. Gravalos, I.; Ziakas, N.; Loutridis, S.; Gialamas, T. A Mechatronic System for Automated Topping and Suckering of Tobacco Plants. *Comput. Electron. Agric.* **2019**, *166*, 104986. [CrossRef]
6. Sharma, K.; Chandel, R. Multiple Attributed Parametric Review on Mechanical Picking of Cotton (*Gossypium Hirsutum* L.) Crop in Relevance to Developing Countries. *AMA Agric. Mech. Asia Afr. Lat. Am.* **2021**, *52*, 7–13.
7. Mhamed, M.; Zhang, Z.; Yu, J.; Li, Y.; Zhang, M. Advances in Apple's Automated Orchard Equipment: A Comprehensive Research. *Comput. Electron. Agric.* **2024**, *221*, 108926. [CrossRef]
8. Nie, J.; Li, Z.; Zhang, Y.; Zhang, D.; Xu, S.; He, N.; Zhan, Z.; Dai, J.; Li, C.; Li, W.; et al. Plant Pruning Affects Photosynthesis and Photoassimilate Partitioning in Relation to the Yield Formation of Field-Grown Cotton. *Ind. Crop. Prod.* **2021**, *173*, 114087. [CrossRef]
9. Wang, P.; Han, X. Development, Analysis, and Verification of an Intelligent Auxiliary Beekeeping Device Mounted on a Crawler Transporter. *Comput. Electron. Agric.* **2023**, *212*, 108148. [CrossRef]
10. Hosfeld, A.; Konigorski, U. A Method for Disturbance-Tolerant "Sensorless" Angle Measurement of DC Motors. *IEEE Trans. Instrum. Meas.* **2022**, *71*, 7501109. [CrossRef]
11. Ramli, R.; Mikami, N.; Takahashi, H. Adaptive Filters for Rotational Speed Estimation of a Sensorless DC Motor with Brushes. In Proceedings of the 10th International Conference on Information Science, Signal Processing and their Applications (ISSPA 2010), Kuala Lumpur, Malaysia, 10–13 May 2010; pp. 562–565.
12. Vazquez-Sanchez, E.; Gomez-Gil, J.; Carlos Gamazo-Real, J.; Fernando Diez-Higuera, J. A New Method for Sensorless Estimation of the Speed and Position in Brushed DC Motors Using Support Vector Machines. *IEEE Trans. Ind. Electron.* **2012**, *59*, 1397–1408. [CrossRef]
13. Radcliffe, P.; Kumar, D. Sensorless Speed Measurement for Brushed DC Motors. *IET Power Electron.* **2015**, *8*, 2223–2228. [CrossRef]
14. Vazquez-Sanchez, E.; Sottile, J.; Gomez-Gil, J. A Novel Method for Sensorless Speed Detection of Brushed DC Motors. *Appl. Sci.* **2017**, *7*, 14. [CrossRef]
15. Nemec, D.; Janota, A.; Hruboš, M.; Šimák, V. Design of an Electronic Odometer for DC Motors. *Transp. Res. Procedia* **2019**, *40*, 405–412. [CrossRef]
16. Texas Instruments: Solving Sensorless Brushed DC Motor Speed and Position Control Using Ripple Counting. 2024. Available online: https://www.ti.com/lit/an/slvafo8a/slvafo8a.pdf (accessed on 15 October 2024).
17. Microchip Technology Inc: Sensorless Position Control of Brushed DC Motor Using Ripple Counting Technique. 2019. Available online: http://ww1.microchip.com/downloads/en/AppNotes/Sensorless-Position-Control-of-Brushed-DC-Motor-Using-Ripple-Counting-Technique-00003049A.pdf (accessed on 15 September 2024).
18. Zhang, Q.; Wen, B.; He, Y. Rotational Speed Monitoring of Brushed DC Motor via Current Signal. *Measurement* **2021**, *184*, 109890. [CrossRef]
19. Vidlak, M.; Gorel, L.; Makys, P.; Stano, M. Sensorless Speed Control of Brushed DC Motor Based at New Current Ripple Component Signal Processing. *Energies* **2021**, *14*, 5359. [CrossRef]
20. Ding, Y.; Ma, Y.; Liu, T.; Zhang, J.; Yang, C. Experimental Study on the Dynamic Stability of Circular Saw Blades during the Processing of Bamboo-Based Fiber Composite Panels. *Forests* **2023**, *14*, 1855. [CrossRef]
21. Yan, B.; Liu, H.; He, F.; Deng, G.; Zheng, S.; Cui, Z.; Zhou, S.; Dai, Y.; Wang, X.; Qin, S.; et al. Analysis and Testing of Pre-Cut Sugarcane Seed Stalk Sawing Performance Parameters. *Agriculture* **2024**, *14*, 953. [CrossRef]
22. Gao, Y.; Wang, Y.; Kang, F.; Kan, J. Multi-Objective Optimization of Cross-Section Integrity Rate and Sawing Power Consumption in Sawing *Caragana Korshinskii Kom.* Branches. *Ind. Crops Prod.* **2023**, *193*, 116244. [CrossRef]
23. Sankarrao, R.; Nayak, D.P.; Pramanick, S. Evaluation of Reduced Torque Ripple in Dodecagonal Voltage Space Vector PWM Fed Open-End Winding Induction Motor Drive. *IEEE Trans. Energy Convers.* **2024**, *39*, 1630–1643. [CrossRef]
24. Yuan, B.; Hu, Z.; Zhou, Z. Expression of Sensorless Speed Estimation in Direct Current Motor with Simplex Lap Winding. In Proceedings of the 2007 International Conference on Mechatronics and Automation, Harbin, China, 5–8 August 2007; pp. 816–821.

25. Vidlak, M.; Makys, P.; Stano, M. Comparison between Model Based and Non-Model Based Sensorless Methods of Brushed DC Motor. *Transp. Res. Procedia* **2021**, *55*, 911–918. [CrossRef]
26. Serna, J.A.d.l.O.; Zamora-Mendez, A.; Mejia-Ruiz, G.E.; Paternina, M.R.A.; Dotta, D.; Lugnani, L.; Garcia, M.; Silva, P.R.D.R. Fast Taylor-Fourier Transform for Monitoring Modern Power Grids With Real-Time Dynamic Harmonic Estimation. *IEEE Trans. Power Deliv.* **2024**, *39*, 2242–2252. [CrossRef]
27. Hosfeld, A.; Hiester, F.; Konigorski, U. Analysis of DC Motor Current Waveforms Affecting the Accuracy of "Sensorless" Angle Measurement. *IEEE Trans. Instrum. Meas.* **2021**, *70*, 7500908. [CrossRef]
28. Khoo, B.; Wee, C.C.; Mariappan, M.; Saad, I. A Hybrid Artificial Intelligence Algorithm to Determine the Speed and Position in Multi Operation Mode Sensorless Brushed D.C. Motor. *Adv. Sci. Lett.* **2017**, *23*, 11374–11377. [CrossRef]
29. Nosheen, T.; Ali, A.; Chaudhry, M.U.; Nazarenko, D.; Shaikh, I.U.H.; Bolshev, V.; Iqbal, M.M.; Khalid, S.; Panchenko, V. A Fractional Order Controller for Sensorless Speed Control of an Induction Motor. *Energies* **2023**, *16*, 1901. [CrossRef]